



Efficient charge separation between UiO-66 and ZnIn₂S₄ flowerlike 3D microspheres for photoelectrochemical properties

Baibai Liu^a, Xinjuan Liu^{a,*}, Junying Liu^b, Chengjie Feng^a, Zhu Li^a, Can Li^a, Yinyan Gong^a, Likun Pan^{c,*}, Shiqing Xu^a, Chang Q. Sun^d

^a Institute of Coordination Bond Metrology and Engineering (CBME), College of Materials Science and Engineering, China Jiliang University, Hangzhou 310018, China

^b Research Center for Combustion and Environment Technology, Shanghai Jiao Tong University, Shanghai 200240, China

^c Shanghai Key Laboratory of Magnetic Resonance, School of Physics and Materials Science, East China Normal University, Shanghai 200062, China

^d School of Electrical and Electronic Engineering, Nanyang Technological University, Singapore 639798, Singapore



ARTICLE INFO

Keywords:

ZnIn₂S₄
UiO-66
Flowerlike 3D microspheres
Co-catalyst
Photoelectrochemical

ABSTRACT

It is still a great challenge to develop efficient semiconductive photocatalysts responding to visible light radiation. We show an efficient ZnIn₂S₄/UiO-66 hybrid photocatalysts with flowerlike 3D microspheres synthesized via a facile solvothermal method. A 20 wt.% UiO-66 emulsion raises the Cr(VI) reduction rate up to 99% and higher after 60 min visible light irradiation. The substantial enhancement of photocatalytic and photoelectrochemical activity of pure ZnIn₂S₄ by UiO-66 addition is attributed to the ZnIn₂S₄/UiO-66 interfacial charge transferring and more active sites for pollutant adsorption.

1. Introduction

Photocatalytic reduction of Cr(VI) to Cr(III) is regarded as an efficient strategy to remove Cr(VI) in dealing with waste water containing heavy metal ions. Intensive efforts have been made on the photocatalysts such as metal oxides, sulphides, oxynitrides, perovskite for Cr (VI) reduction. However, the Cr(VI) reduction rate is limited due to the narrow window of light absorption and quick recombination rate of charge carriers. Therefore, developing high efficiency visible-light photocatalysts to meet industrial needs remains a challenge [1,2].

Metal organic frameworks (MOFs) have attracted considerable attention owing to their high specific surface area, tunable pore size, functionalities and designable framework structures as well as wide applications in catalysis, separation, chemical sensors, gas storage, drug delivery and biomedicine [3,4]. Undercoordinated atoms at site of point defects, terrace edges, and nanostructure of various shapes and hetero-coordinated atoms of doping, alloying and at the interfaces provide excessive electrons or holes promoting catalytic reaction [5,6]. Bond contraction and bond nature alteration modulate interatomic interaction and cause local electron entrapment and polarization, which serve as carrier for the acceptor-type and donor-type catalysts [7,8].

Since 2007 when Garcia et al. [9] firstly proved that MOF-5 can serve as a photocatalyst with excellent activity in the degradation of phenol, MOFs have been extensively studied for photocatalytic degradation of organic pollutants (as MOF-5, NTU-9, MIL-53(Fe), MIL-

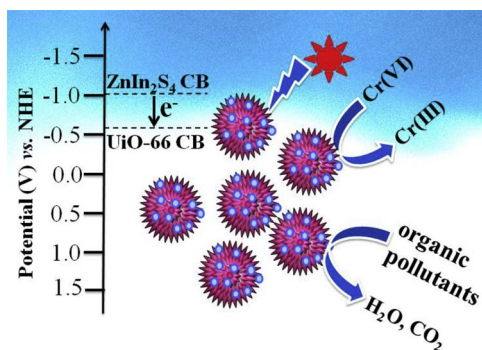
100(Fe), MIL-88A, ZIF-8) [10], reduction CO₂ (as NH₂-MIL-125(Ti), NH₂-UiO-66, UiO-67, MOF-253, MIL-53(Fe)) [11], and water splitting to produce hydrogen (as UiO-66, Ti-MOF-NH₂) [12]. The metal centers in MOFs can serve as quantum dots and the organic linkers as antenna to excite the metal clusters in the catalytic process.

Among these MOFs, UiO-66 as typical Zr-based MOFs possesses superior thermostability, extraordinary chemical and structural stability to water, which makes it a promising candidate of photocatalyst [13]. Unfortunately, UiO-66 fails to satisfactory activity owing to the limited light absorption. A series of strategies has been carried out towards higher visible light catalytic activity of UiO-66, such as modifying on the metal clusters/functional organic ligands for more visible light absorption and reactant adsorption, and coupling with different semiconductor/noble metal nanoparticles for better charge separation and reactant activation [14]. Recent efforts have demonstrated that the amine functionalized MOFs can extend the absorption to visible light region, because the amine group can improve both the electron transfer from the excited amine functionalized organic linker to oxo-metal clusters and from the direct excitation of oxo-metal cluster [15,16]. UiO-66-based composites such as UiO-66-Bi₂WO₆, BiOBr, g-C₃N₄, CdS, AgI, Ag₂CO₃, MoS₂, etc., exhibit excellent catalytic activity due to their synergistic effect under visible light irradiation [17]. However, few efforts have been made to the application of UiO-66 for photocatalytic reduction of Cr(VI).

As an important ternary metal chalcogenide semiconductor, ZnIn₂S₄

* Corresponding authors.

E-mail addresses: lxj669635@126.com (X. Liu), lkpan@phy.ecnu.edu.cn (L. Pan).



Scheme 1. Proposed visible light photocatalytic mechanism for ZU hybrids.

with narrow bandgap (2.34–2.48 eV) has attracted broad interest for visible light photocatalytic evolution hydrogen and degradation of organic pollutants [18]. The catalytic ability of pure ZnIn_2S_4 is lower than expected because of the poor absorption and short lifetime of charge carries [19]. Many efforts have been made to improve the catalytic activity, including controlling morphologies, doping noble metal and constructing heterostructures composites [20]. Constructing 0–3D heterostructures is an effective method to enhance the catalytic activity of pure ZnIn_2S_4 [21,22]. Therefore, it is highly desirable to fabricate the $\text{ZnIn}_2\text{S}_4/\text{UiO-66}$ (ZU) hybrid photocatalysts, which can efficiently increase the visible light absorption and boost the separation of charge carries, improving the catalytic activity due to the stepwise structure of band-edge levels constructed in the ZU hybrid photocatalysts with flowerlike 3D microspheres (Scheme 1). From the band structure viewpoint, the position of conduction band (CB) of ZnIn_2S_4 (−1.0 vs. NHE) is more negative than that of UiO-66 (−0.6 vs. NHE) [23], thus the photo-induced electrons can be efficiently transferred from ZnIn_2S_4 to UiO-66 . Unfortunately, there appears little exploration on the ZU hybrid photocatalysts, especially in terms of photocatalytic reduction of $\text{Cr}(\text{VI})$.

We present herein a fast strategy for synthesizing the ZU hybrid photocatalysts with flowerlike microspheres via a hydrothermal method for $\text{Cr}(\text{VI})$ reduction. The Electronic Supplementary Information (ESI†) describes the experimental procedures. ZU-10, ZU-20 and ZU-30 represent for the ZU with 10, 20 and 30 wt.% UiO-66 , respectively. The ZU hybrid displays higher visible light catalytic activity than either ZnIn_2S_4 or UiO-66 alone.

2. Results and discussion

2.1. Characterizations

The X-ray powder diffraction (XRD) patterns of pure ZnIn_2S_4 , UiO-66 , ZU-10, ZU-20 and ZU-30 are shown in Fig. 1. All diffraction peaks in the XRD pattern of pure ZnIn_2S_4 can be indexed as hexagonal ZnIn_2S_4 (JCPDS 65-2023) [24]. No additional impurity peaks are detected, demonstrating the good purity of ZnIn_2S_4 . The XRD diffraction pattern of pure UiO-66 can be assigned to the crystallographic UiO-66 phase, in agreement with the literature [25]. For the ZU hybrid, the main diffraction peaks are similar to those of pure ZnIn_2S_4 , indicating that the presence of UiO-66 does not result in the development of new crystal orientations or change in preferential orientations of ZnIn_2S_4 . Compared with pure ZnIn_2S_4 , the new peaks corresponding to the crystallographic UiO-66 phase appear in XRD patterns of ZU hybrid, which confirms the existence of UiO-66 in the ZU hybrid. With the increase of UiO-66 content, the intensity of diffraction peaks for UiO-66 increases, demonstrating that more UiO-66 is introduced into the ZU hybrid.

Fig. 2(a) and (b) shows the field-emission scanning electron microscopy (FESEM) images of pure ZnIn_2S_4 and UiO-66 . Pure ZnIn_2S_4 is composed of a large quantity of flowerlike microspheres with an average diameter of about 5 μm , which is made up of numerous

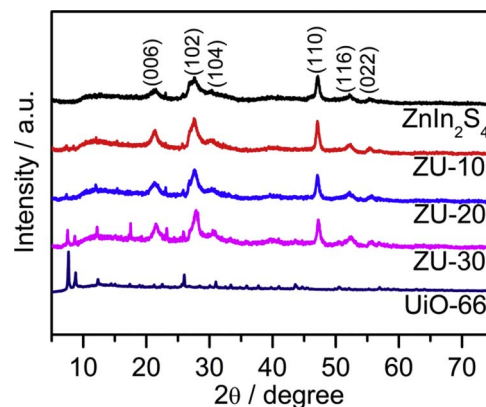


Fig. 1. XRD patterns of pure ZnIn_2S_4 , UiO-66 , ZU-10, ZU-20 and ZU-30.

interweaving petals. It can be found from Fig. 2(b) that the as-prepared UiO-66 nanoparticles are uniform with an average size of 50 nm. The FESEM images of ZU-10 and ZU-30 are shown in Fig. 2(c) and (d). The morphology of ZU-20 (not shown here) is similar to that of ZU-10 and ZU-30. When the UiO-66 is introduced into the pure ZnIn_2S_4 , UiO-66 nanoparticles are well dispersed into ZnIn_2S_4 flowerlike microspheres, forming a good contact that favors the fast transport of charge carriers in catalytic reaction process.

More detailed structural analysis of ZU hybrid was carried out using high-resolution transmission electron microscopy (HRTEM). Fig. 3(a–c) shows the low- and high-magnification HRTEM images of ZU-20. Some individual microspheres with a zigzag circle are observed, in accordance with the FESEM images. As shown in Fig. 3(b) and (c), the flowerlike microspheres are self-assembled by ZnIn_2S_4 petals, and UiO-66 nanoparticles are embedded into the ZnIn_2S_4 petals. Moreover, the lattice interplanar spacing is measured to be 0.32 nm, corresponding to the (102) plane of hexagonal ZnIn_2S_4 (JCPDS 65-2023) (Fig. 3(d)) [26].

Based on above experimental results, a possible formation mechanism of ZU hybrid with flowerlike microspheres is proposed as follows (Scheme 2). The thioacetamide (TAA) plays an important role in the formation process of ZU hybrid. TAA can be used as a chelating agent. When the UiO-66 , $\text{Zn}(\text{NO}_3)_3$, $\text{In}(\text{NO}_3)_3$ and TAA were dissolved into deionized water, Zn^{2+} and In^{2+} cations coordinated with TAA to form $\text{Zn}(\text{TAA})_n^{2+}$ and $\text{In}(\text{TAA})_n^{2+}$ in the solution (Eqs. (1) and (2)) [27]. Meanwhile, the TAA was decomposed to release gradually the S^{2-} ions at higher temperatures (Eqs. (3)–(5)), which combined with $\text{Zn}(\text{TAA})_n^{2+}$ and $\text{In}(\text{TAA})_n^{2+}$ to form ZnIn_2S_4 nuclei (Eq. (6)).



In initial stage, the ZnIn_2S_4 nuclei was accelerated to form tiny nanoparticles, and then self-assembled via two or three dimensional growth to form the petals [28]. The UiO-66 nanoparticles were embedded into the ZnIn_2S_4 petals. Subsequently, these petals undergone curvature owing to surface tension at high temperature, and were self-assembled to from the flowerlike microspheres [29]. Moreover, the long reaction time and higher temperature in a sealed autoclave can promote the crystal growth from hexagonal ZnIn_2S_4 .

Fig. 4 shows the Fourier transform infrared spectroscopy (FTIR) spectra of pure ZnIn_2S_4 , UiO-66 , ZU-10, ZU-20 and ZU-30. For pure ZnIn_2S_4 , the absorption peaks around 1610 and 1396 cm^{-1} for all the samples corresponded to the surface absorbed water molecules and

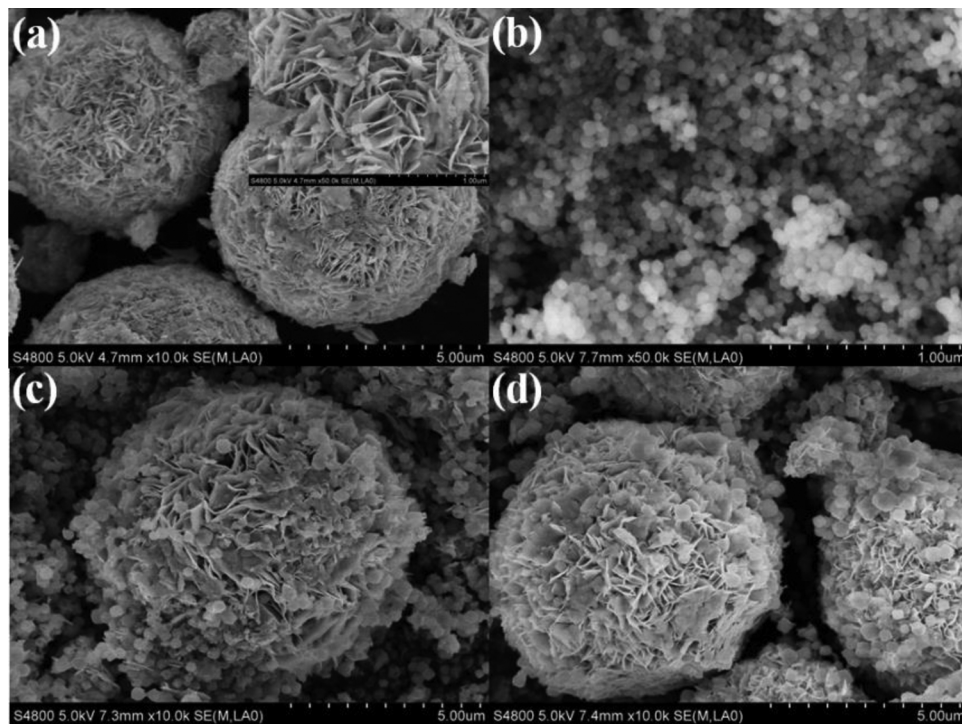


Fig. 2. FESEM images of (a) pure ZnIn_2S_4 , (b) UiO-66, (c) ZU-10 and (d) ZU-30.

hydroxyl groups [30]. For UiO-66, the bands at 1577 and 1398 cm^{-1} are recognized as the O—C—O asymmetric and symmetric stretching in the terephthalic acid (BDC) ligand [31]. The weak band at 1506 cm^{-1} is identified as the C=C of a benzene ring. The 814, 746 and 667 cm^{-1} bands are associated with the O—H and C—H vibration in the BDC ligand. The band at 552 cm^{-1} is linked to the Zr-(OC) asymmetric stretch [31]. Compared with pure ZnIn_2S_4 , new absorption peaks ascribed to UiO-66 appear in the FTIR spectra of ZU hybrid, which also proves the existence of UiO-66 in the ZU hybrid.

The chemical status and surface chemical composition of ZU-10 were characterized by X-ray photoelectron spectroscopy (XPS) measurement. Fig. 5 shows the high-resolution XPS spectra of Zn 2p, In 3d,

S 2p and Zr 3d. The Zn 2p spectrum splits up to two peaks at 1021.6 eV and 1044.7 eV (Fig. 5(a)), which corresponds to the Zn 2p_{3/2} and Zn 2p_{1/2}, respectively [32]. As shown in Fig. 5(b), two peaks at 444.8 eV and 452.3 eV are assigned to the In 3d_{5/2} and In 3d_{3/2} of ZnIn_2S_4 , respectively, which is similar to those reported in the literature [33]. The S 2p spectrum in Fig. 5(c) can be fitted into two peaks at 160.9 eV and 162.1 eV, which are ascribed to S 2p_{3/2} and S 2p_{1/2}, respectively [34]. The Zr 3d spectrum in Fig. 5(d) can be deconvoluted into two peaks locating at 182.2 eV and 184.5 eV for Zr 3d_{5/2} and Zr 3d_{3/2}, respectively, which indicates the existence of Zr^{6+} for the zirconium-oxo cluster [31]. All Results indicate the existence of chemical states of Zn^{2+} , In^{3+} and S^{2-} . No other peaks corresponding to impurities are

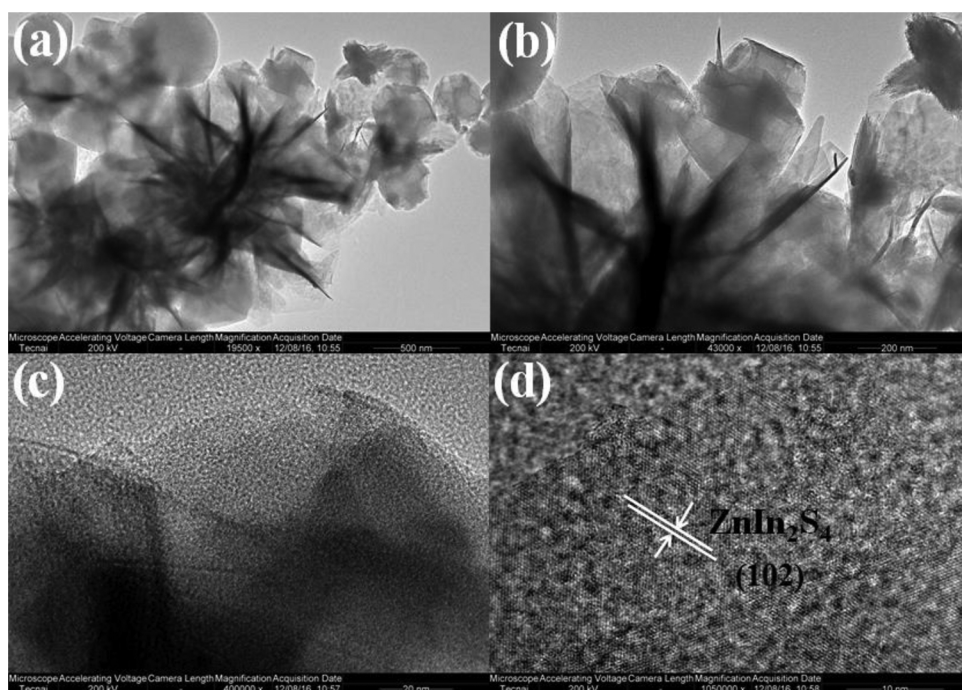


Fig. 3. (a-b) Low- and (c-d) high-magnification HRTEM images of ZU-10.



Scheme 2. Schematic illustration of the possible formation mechanism of ZU hybrid with flowerlike microspheres.

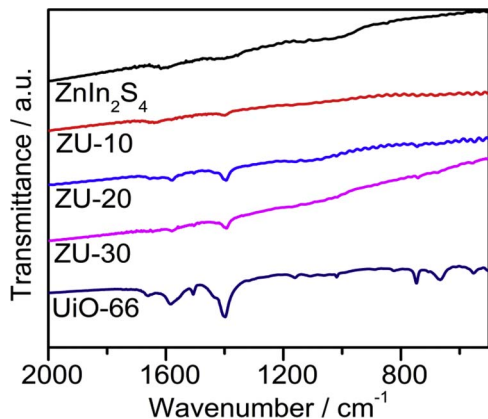


Fig. 4. FTIR spectra of pure ZnIn_2S_4 , UiO-66 , ZU-10, ZU-20 and ZU-30.

observed.

The UV-vis spectra of pure ZnIn_2S_4 , UiO-66 , ZU-10, ZU-20 and ZU-30 are shown in Fig. 6. As seen, UiO-66 has good absorption in the UV light region, while pure ZnIn_2S_4 displays good visible light absorption due to its narrow bandgap. Compared with pure ZnIn_2S_4 , the absorption of ZU hybrid with an appropriate proportion of UiO-66 (ZU-10 and ZU-

20) does not show a clear change. When the UiO-66 content surpasses 20%, the absorption of ZU hybrid decreases, which is not beneficial to the catalytic process. In addition, the band gap values of all samples obtained by transformation based on the Kubelka-Munk function versus the energy of light are 1.86, 1.84, 1.88 and 1.92 eV for pure ZnIn_2S_4 , ZU-10, ZU-20 and ZU-30, respectively (Fig. 6(b)).

2.2. Photocatalytic activity and photocurrent response

Photocatalytic activity of pure ZnIn_2S_4 , UiO-66 and ZU hybrids was performed in the reduction of Cr(VI) under visible light irradiation. The photoreduction activity in the Cr(VI) solution was recorded by the UV-vis absorption spectroscopy, and the temporal changes of Cr(VI) concentration were monitored by recording the variations of maximum absorption of Cr(VI) at 365 nm [35]. Fig. 7(a) shows the time-resolved absorption spectra of Cr(VI) with ZU-20 under visible light irradiation. Furthermore, the concentrations of HCrO_4^- ions also were determined colorimetrically at 540 nm using the diphenylcarbazide (DPC) method [36], as shown in Fig. S1. It can be observed that the absorption peaks of Cr(VI) decrease with the increase of irradiation time, demonstrating that the Cr(VI) concentration decreases in the catalytic process.

Fig. 7(b) displays the time-dependent reduction rates of Cr(VI) by pure ZnIn_2S_4 , UiO-66 , ZU-10, ZU-20 and ZU-30 under visible light irradiation. The research progress of MOFs applications in photocatalytic reduction of Cr(VI) was highlighted as listed in Table S1. It can be observed that MOFs-based composites exhibit excellent catalytic activity in the reduction of Cr(VI), and the Cr(VI) reduction rates of higher than 97% have been achieved under visible light irradiation. However, only low concentration Cr(VI) was studied in these reports. Herein, we carried out the photocatalytic reduction of Cr(VI) experiment in high concentration Cr(VI) solution with 80 mg l^{-1} . The blank experiment indicates that the variation of Cr(VI) concentration is negligible without photocatalyst under visible light irradiation. For pure UiO-66 , a very low reduction rate of Cr(VI) is observed due to the limited light absorption, while pure ZnIn_2S_4 shows an obviously higher reduction rate of 77% after 60 min irradiation. As discussed above, the introduction of UiO-66 makes important effects on the light absorption, specific surface areas and charge transfer behavior of ZU hybrid photocatalysts.

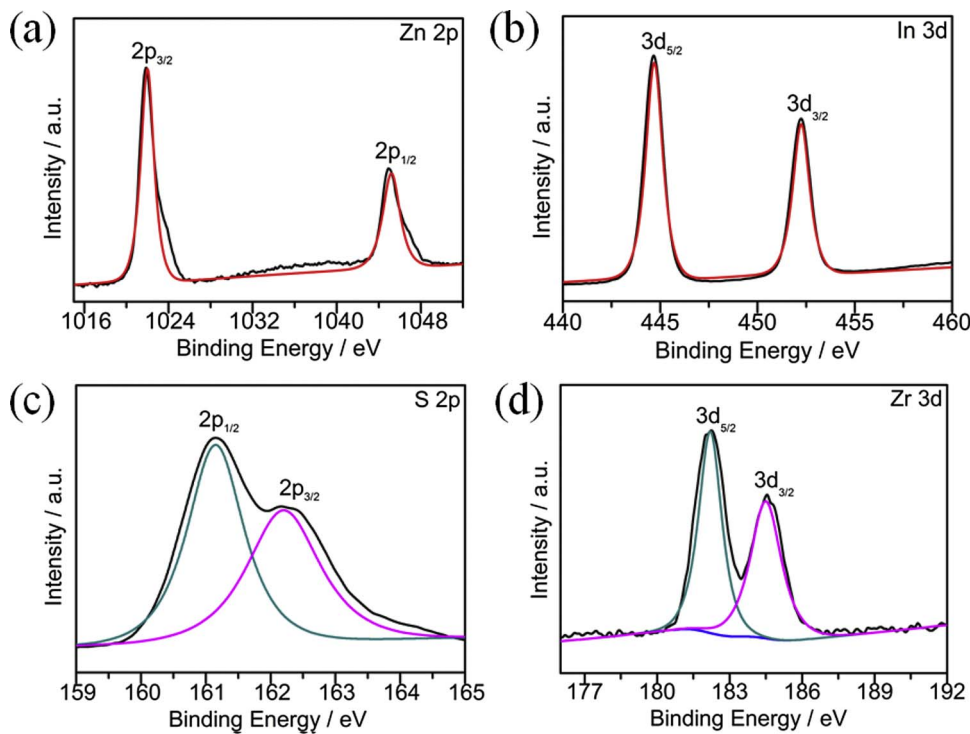
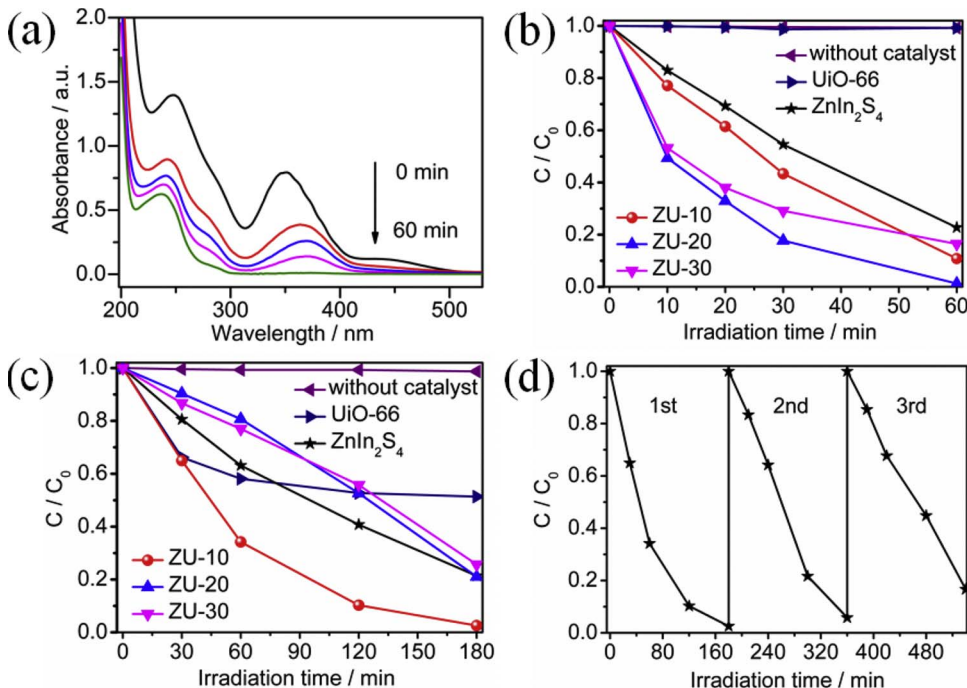
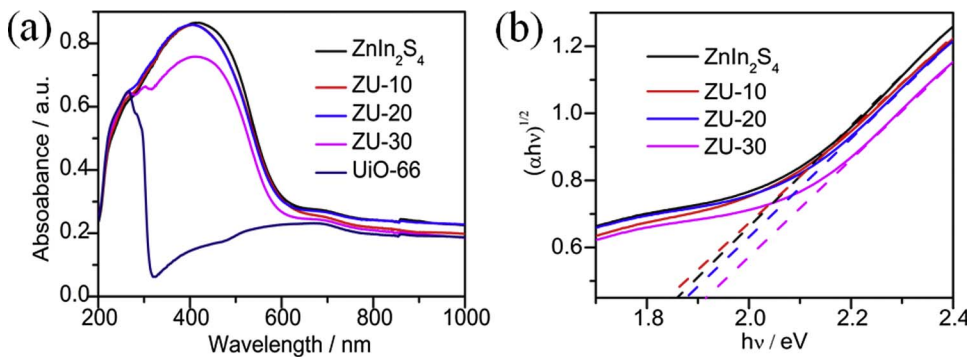


Fig. 5. XPS spectra of (a) Zn 2p, (b) In 3d, (c) S 2p and (d) Zr 3d for ZU-10.



Therefore, it is inevitable to further affect their catalytic activity. When the $\text{UiO}-66$ is introduced into ZnIn_2S_4 forming hybrid, the Cr(VI) reduction rates gradually improve. The Cr(VI) reduction rates are 90%, 99% and 84% for ZU-10, ZU-20 and ZU-30 after 60 min irradiation, respectively. The reduction rates of Cr(VI) obtained by DPC method are 79%, 96%, 99% and 89% for ZnIn_2S_4 , ZU-10, ZU-20 and ZU-30 after 60 min irradiation, respectively. The turnover numbers of photocatalytic production in the reduction of Cr(VI) are 0.35, 0.46, 0.57 and 0.55 for pure ZnIn_2S_4 , ZU-10, ZU-20 and ZU-30, respectively.

The kinetics of Cr(VI) reduction were found to fit between pseudo-first-order kinetic equation and experimental data, as shown in Fig. S2(a). The values of rate constants in the Cr(VI) reduction process are 0.02495, 0.00015, 0.02495, 0.07234 and 0.03745 min^{-1} for pure ZnIn_2S_4 , $\text{UiO}-66$, ZU-10, ZU-20 and ZU-30, respectively. The catalytic activity follows the increasing order of ZU-20 > ZU-10 > ZU-30 > ZnIn_2S_4 > $\text{UiO}-66$. The ZU hybrids exhibit better visible-light-driven catalytic activity for Cr(VI) reduction than that of pure ZnIn_2S_4 and $\text{UiO}-66$. With the increase of $\text{UiO}-66$ content, the Cr(VI) reduction rate increases greatly and then decreases when the $\text{UiO}-66$ content surpasses 20%. ZU-20 hybrid exhibits a best photocatalytic activity in the reduction of Cr(VI) under visible light irradiation. Results indicate that the $\text{UiO}-66$ content has important effects on the catalytic activity of ZU hybrids in the reduction of Cr(VI), and the optimum $\text{UiO}-66$ content is 20% under the present photocatalytic system.

Photocatalytic degradation of methyl orange (MO) by pure ZnIn_2S_4 ,

Fig. 6. (a) UV-vis spectra of pure ZnIn_2S_4 , $\text{UiO}-66$, ZU-10, ZU-20 and ZU-30; (b) the plot of transformed Kubelka-Munk function versus the energy of light.

Fig. 7. (a) UV-vis absorbance of Cr(VI) with the variation of irradiation time; Photocatalytic (b) reduction of Cr(VI) and (c) degradation of MO by pure ZnIn_2S_4 , $\text{UiO}-66$, ZU-10, ZU-20 and ZU-30 under visible light irradiation; (d) photo-stability of ZU-10.

$\text{UiO}-66$ and ZU hybrids were also investigated under visible light irradiation, as shown in Fig. 7(c). It can be observed that the degradation rates are 79%, 49%, 98%, 80% and 75% for pure ZnIn_2S_4 , $\text{UiO}-66$, ZU-10, ZU-20 and ZU-30 after 180 min irradiation, respectively. The turnover numbers of photocatalytic production in the degradation of MO are 0.12, 0.16, 0.15 and 0.15 for pure ZnIn_2S_4 , ZU-10, ZU-20 and ZU-30, respectively. In the photocatalytic degradation of MO process, the values of rate constants are 0.00845, 0.00313, 0.0206, 0.00848 and 0.00727 min^{-1} for pure ZnIn_2S_4 , $\text{UiO}-66$, ZU-10, ZU-20 and ZU-30, respectively (Fig. S2(b)). Similarly, the degradation activity depends on the $\text{UiO}-66$ content in the ZU hybrid photocatalysts. The ZU-10 hybrid photocatalysts shows the highest rate constant in the degradation of MO process.

The photo-stability of photocatalysts is very important for its practical application. Therefore, the photo-stability of ZU hybrid (ZU-10) was evaluated by repeatedly photocatalytic degradation of MO experiment with three times under visible light irradiation (Fig. 7(d)). As shown in Table S2, the degradation rate decreases to 84% after three cycles, which may be due to the loss of photocatalyst during collection process [37]. Similar results are also found in Fig. S3 and Table S2 for ZU-20 in the reduction of Cr(VI) under visible light irradiation, which is consistent with the observed results in the literature [38,39]. The decreased reduction rate is ascribe to the deposition of chromium compounds on surface of photocatalysts and the loss of photocatalyst during collection process [37]. Moreover, the surface chemical composition

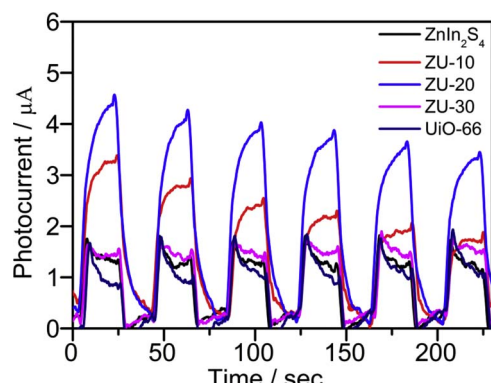


Fig. 8. Photocurrent responses of pure ZnIn_2S_4 , UiO-66 , ZU-10, ZU-20 and ZU-30 under visible light irradiation.

and crystal structure of ZU-10 hybrid after the photocatalytic reaction were characterized by XPS and XRD (Figs. S4 and S5). It can be observed that the binding energy of Zn, In, S and Zr did not exhibit obvious changes before and after the photocatalytic reaction. The crystal structure of ZU-10 hybrid after photocatalytic reaction is similar to that of ZU-10 before photocatalytic reaction. Results indicate that the as-prepared ZU hybrids are relatively stable, and can be regard as a promising visible light photocatalysts in practical application.

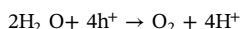
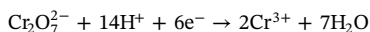
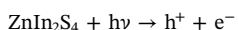
It is known that during photocatalysis, the charge transportation and separation is crucial factors that determines catalytic activity, which can be demonstrated by the photocurrent responses. Fig. 8 shows the photocurrent responses of pure ZnIn_2S_4 , UiO-66 , ZU-10, ZU-20 and ZU-30 under visible light irradiation. It can be found that the photocurrent quickly decreases to zero when the light is switched off, indicating the recombination of photo-induced electron and hole. The transient photocurrent responses of all samples are reversible and relatively stable at light-on and light-off. Compared with pure ZnIn_2S_4 and UiO-66 , ZU hybrids show higher photocurrent due to the stepwise structure of band-edge levels constructed in the ZU hybrids. ZU-20 exhibits the highest photocurrent, revealing more efficient charge transfer process and longer lifetime of the photo-induced electron-hole pairs.

2.3. Possible photocatalytic mechanism

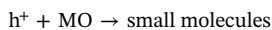
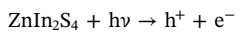
The possible photocatalytic mechanisms in the reduction of Cr(VI) and degradation of MO are proposed, as shown in Scheme 1. Under visible light irradiation, the valance band (VB) electrons of ZnIn_2S_4 can be excited to the CB to generate the electron-hole pairs. Subsequently, the electrons and holes migrate to the surface of photocatalysts to participate in redox reactions. Meanwhile, the electrons and holes may recombine in the bulk and surface of the photocatalysts.

In the photocatalytic reduction of Cr(VI) process, the Cr(VI) can be reduced to Cr(III) by photo-induced electrons, which is because that the Cr(VI)/Cr(III) potential (0.51 V vs. NHE [40]) is more positive than the CB of ZnIn_2S_4 (-1 V vs. NHE). The photocatalyst (ZU-20) after photocatalytic reaction was characterized by XPS to detect the reductive product. Fig. S6 shows the high resolution XPS spectrum of Cr 2p for ZU-20 after the photocatalytic reaction. Two peaks located at 577.3 and 586.9 eV correspond to Cr 2p_{1/2} and Cr 2p_{3/2} orbitals, respectively, which are attributed to Cr(VI) and Cr(III). Result demonstrates the existence of Cr(VI) and Cr(III) on the surface of ZU-20. Trapping experiment was carried out to demonstrate the role of photo-induced electrons, as shown in Fig. S7. Results indicate that the addition of electron scavengers leads to a rapid decrease in the catalytic activity, demonstrating that the photo-induced electrons play an important role in the catalytic reduction of Cr(VI) process. Furthermore, the photo-induced holes can oxidize the H_2O to form O_2 , which was proved by gas

chromatograph measurement in our previous works [41]. The major reaction steps are summarized as follows:

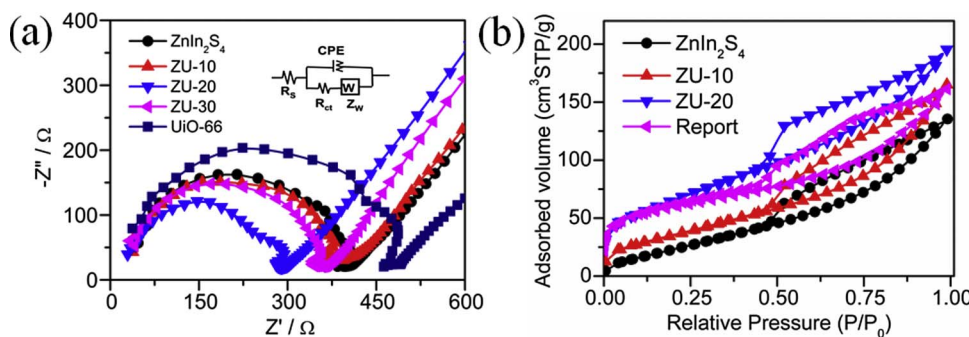


In the photocatalytic degradation of MO process, the holes contribute to the oxidative pathways for photocatalytic degradation reaction. Moreover, the VB of ZnIn_2S_4 (1.6 V vs. NHE) is negative than the $\cdot\text{OH}/\text{H}_2\text{O}$ potential (2.27 V, vs. NHE), thus the holes cannot oxide H_2O to form $\cdot\text{OH}$, which is confirmed by the photoluminescence method using coumarin as a probe molecule [42]. As shown in Fig. S8, trapping experiment demonstrates that the $\cdot\text{OH}$ has a negligible effect, and the holes play a dominant role in the photocatalytic degradation of MO process. The final products were determined by high-resolution mass spectrometer using Bruker micro TOF-Q II, as shown in Fig. S9. Results indicate that there is some degradation byproducts variably presented at the various times. Before light irradiation, the sample shows two m/z peaks at 328 corresponding to parent dye molecule [43] and at 307 attributing to the loss of one methyl group from nitrogen atom of amino group [44]. After 60 min irradiation, their intension quickly decreases. A new byproduct with m/z peak at 320 is observed, corresponding to the monohydroxylated product of MO [44,45]. After 180 min irradiation, the intension of m/z peaks at 307, 328 and 320 reaches the minimum closely to zero. However, the main byproducts with m/z peaks at 243 and 274 are found, corresponding to $[\text{M} - \text{H} - \text{SO}_2]^{-1}$ and $[\text{M} - \text{H} - \text{CH}_3]^{-1}$, respectively [44,45]. Furthermore, the m/z peak at 147 always exists, and the intensity hardly changes in the catalytic degradation process, which belongs to the impurity in the MO solution [44]. The major reaction steps are summarized as follows:



Unfortunately, pure ZnIn_2S_4 shows poor catalytic activity in the reduction of Cr(VI) due to the quick recombination of charge carries. Based on the stepwise structure of band-edge levels constructed in the ZU hybrids, the introduction of UiO-66 can enhance the separation and transfer efficiency of photo-induced charge carries and prolong their lifetime, which could be evaluated by the electrochemical impedance spectra (EIS) under visible light irradiation. The typical Nyquist plots of pure ZnIn_2S_4 , UiO-66 , ZU-10, ZU-20 and ZU-30 are shown in Fig. 9(a). The semicircle is associated with the charge transfer resistance (R_{ct}) and constant phase element (CPE) at the photocatalyst/electrolyte interface. The inclined line corresponds to the ion diffusion process in the electrolyte, arising from the Warburg impedance Z_w . The values of R_s , R_{ct} and CPE are fitted according to the equivalent circuit (inset of Fig. 9(a)) and listed in Table S3. The smaller semicircle radius shows a more efficient transfer of photo-induced charge carries. It can be observed that the semicircle radius of ZU hybrids is smaller than that of pure ZnIn_2S_4 and UiO-66 , demonstrating that the introduction of UiO-66 can inhibit the recombination of photo-induced charge carries, in accordance with the result of photocurrent responses. Moreover, with the increase of UiO-66 content, the semicircle radius decreases and then increases. EIS and photocurrent responses results demonstrate that ZU-20 shows the highest separation efficiency of photo-induced charge carries, in agreement with the result of photocatalytic experiment.

Beside the recombination of photo-induced charge carries, the adsorption is also crucial factor in the photocatalytic process, which was evaluated by nitrogen adsorption-desorption isotherms (Fig. 9(b)). All pure ZnIn_2S_4 and ZU hybrids display type IV isotherms with H_2 and H_3 hysteresis loops, demonstrating the presence of mesopores. The Brunauer-Emmett-Teller specific surface area, pore volumes and average pore size of pure ZnIn_2S_4 and ZU hybrids are listed in Table S4. ZU hybrids have higher specific surface areas than pure ZnIn_2S_4 due to high



surface areas of UiO-66, which can provide more active sites, consequently enhance the catalytic activity. However, when the UiO-66 content is further increased (ZU-30), the specific surface area decreases, which may be due to the blocking of pores by the stacked UiO-66 in the composites [46–50].

Based on the above results, the enhanced mechanism of ZU hybrids is proposed. During the photocatalytic process, the photo-induced electrons can transfer from the ZnIn₂S₄ CB to UiO-66 CB due to their synergistic effect, which can improve the separation efficiency and prolong the lifetime of photo-induced charge carries that proved by EIS and photocurrent responses, thus enhancing the catalytic activity. Furthermore, the introduction of UiO-66 increase the specific surface areas of ZU hybrids that proved by nitrogen adsorption-desorption isotherms, which is beneficial to the catalytic reaction. Therefore, the enhancement of catalytic activity for ZU hybrids arises from more active sites and the reduced recombination of charge carries with the introduction of UiO-66. Moreover, the photo-induced electrons dominant the Cr(VI) reduction process, while the holes play an important role in the MO degradation process.

3. Conclusions

In summary, a series of ZU hybrids with flowerlike 3D microspheres were prepared via a facile solvothermal method for catalysis. Results indicate that the ZU hybrid displays excellent catalytic activity due to their synergistic effect. The catalytic rates in Cr(VI) reduction and MO degradation higher than 97% have been achieved with 20 and 10 wt.% UiO-66 emulsions under visible light irradiation. The enhanced catalytic activity is ascribed to more active sites and efficient charge transfer with the introduction of UiO-66. It is expected that our work could provide valuable information on the design of MOFs-based composites with further desirable properties.

Acknowledgements

Financial support from the National Natural Science Foundation of China (No. 21401180, 51402274 and 51402277), Province Natural Science Foundation of Zhejiang (No. LY18E060005 and LY18E020007), Undergraduate Scientific and Technological Innovation Project of Zhejiang Province (No. 2017R409032), National Undergraduate Innovation and Entrepreneurship Project of China (No. 201710356021) are gratefully acknowledged.

Appendix A. Supplementary data

Supplementary data associated with this article can be found, in the online version, at <https://doi.org/10.1016/j.apcatb.2017.12.052>.

References

Fig. 9. (a) Nyquist plots and (b) Nitrogen adsorption-desorption isotherms of pure ZnIn₂S₄, UiO-66, ZU-10, ZU-20 and ZU-30. Inset is the corresponding equivalent circuit model.

- [1] X.C. Zhang, T.Y. Guo, X.W. Wang, Y.W. Wang, C.M. Fan, H. Zhang, Facile composition-controlled preparation and photocatalytic application of BiOCl/Bi₂O₃ nanosheets, *Appl. Catal. B: Environ.* 150 (2014) 486–495.
- [2] X.Q. Hao, Z.L. Jin, H. Yang, G.X. Lu, Y.P. Bi, Peculiar synergistic effect of MoS₂ quantum dots and graphene on Metal-Organic Frameworks for photocatalytic hydrogen evolution, *Appl. Catal. B: Environ.* 210 (2017) 45–56.
- [3] M.C. Wen, K. Mori, Y. Kuwahara, H. Yamashita, Plasmonic Au@Pd nanoparticles supported on a basic metal-organic framework: synergic boosting of H₂ production from formic acid, *ACS Energy Lett.* 2 (2017) 1–7.
- [4] X.J. Liu, X. Zhang, M.L. Bo, L. Li, H.W. Tian, Y.G. Nie, Y. Sun, S.Q. Xu, Y. Wang, W.T. Zheng, C.Q. Sun, Coordination-resolved electron spectrometrics, *Chem. Rev.* 115 (2015) 6746–6810.
- [5] L. Li, F.L. Meng, X.Y. Hu, L. Qiao, C.Q. Sun, H.W. Tian, W.T. Zheng, Nitrogen mediated electronic structure of the Ti(0001) surface, *RSC Adv.* 6 (2016) 14651–14657.
- [6] C.Q. Sun, Y. Wang, Y.G. Nie, B.R. Mehta, M. Khanuja, S.M. Shivaprasad, Y. Sun, J.S. Pan, L.K. Pan, Z. Sun, Interface quantum trap depression and charge polarization in the CuPd and AgPd bimetallic alloy catalysts, *Phys. Chem. Chem. Phys.* 12 (2010) 3131–3135.
- [7] C.Q. Sun, Y. Wang, Y. Nie, Y. Sun, J. Pan, L. Pan, Z. Sun, Adatoms-induced local bond contraction quantum trap depression, and charge polarization at Pt and Rh surfaces, *J. Phys. Chem. C* 113 (2009) 21889–21894.
- [8] M. Alvaro, E. Carbonell, B. Ferrer, F.X. Llabrési Xamena, H. Garcia, Semiconductor behavior of a metal-organic framework (MOF), *Chem. Eur. J.* 13 (2007) 5106–5112.
- [9] J.X. Liu, R. Li, Y.Y. Hu, T. Li, Z.H. Jia, Y.F. Wang, Y.W. Wang, X.C. Zhang, C.M. Fan, Harnessing Ag nanofilm as an electrons transfer mediator for enhanced visible light photocatalytic performance of Ag@AgCl/Ag nanofilm/ZIF-8 photocatalyst, *Appl. Catal. B: Environ.* 202 (2017) 64–71.
- [10] D.R. Sun, Y. Fu, W. Liu, L. Ye, D. Wang, L. Yang, X. Fu, Z. Li, Studies on photocatalytic CO₂ reduction over NH₂-UiO-66(Zr) and its derivatives: towards a better understanding of photocatalysis on metal-organic frameworks, *Chem. Eur. J.* 19 (2013) 14279–14285.
- [11] Y. Chen, L. Tan, J. Liu, S. Qin, Z. Xie, J. Huang, Y. Xu, L. Xiao, C. Su, Calix[4] arene based dye-sensitized Pt@UiO-66-NH₂ metal-organic framework for efficient visible-light photocatalytic hydrogen production, *Appl. Catal. B: Environ.* 206 (2017) 426–433.
- [12] M. Wen, K. Mori, Y. Kuwahara, T.C. An, H. Yamashita, Design and architecture of metal organic frameworks for visible light enhanced hydrogen production, *Appl. Catal. B: Environ.* 218 (2017) 555–569.
- [13] Y. Li, H. Xu, S.X. Ouyang, J.H. Ye, Metal-organic frameworks for photocatalysis, *Phys. Chem. Chem. Phys.* 18 (2016) 7563–7572.
- [14] C. Wang, X. Du, J. Li, X. Guo, P. Wang, J. Zhang, Photocatalytic Cr(VI) reduction in metal-organic frameworks: a mini-review, *Appl. Catal. B: Environ.* 193 (2016) 198–216.
- [15] L.J. Shen, W.M. Wu, R.W. Liang, R. Lin, L. Wu, Highly dispersed palladium nanoparticles anchored on UiO-66(NH₂) metal-organic framework as a reusable and dual functional visible-light-driven photocatalyst, *Nanoscale* 5 (2013) 9374–9382.
- [16] L.J. Shen, M.B. Luo, Y.H. Liu, R.W. Liang, F.F. Jing, L. Wu, Noble-metal-free MoS₂ co-catalyst decorated UiO-66/CdS hybrids for efficient photocatalytic H₂ production, *Appl. Catal. B: Environ.* 166 (2015) 445–453.
- [17] L. Shang, C. Zhou, T. Bian, H.J. Yu, L.Z. Wu, C.H. Tung, T.R. Zhang, Facile synthesis of hierarchical ZnIn₂S₄ submicrospheres composed of ultrathin mesoporous nanosheets as a highly efficient visible-light-driven photocatalyst for H₂ production, *J. Mater. Chem. A* 1 (2013) 4552–4558.
- [18] Y.J. Chen, G.H. Tian, W. Zhou, Y.T. Xiao, J. Wang, X. Zhang, H.G. Fu, Enhanced photogenerated carrier separation in CdS quantum dot sensitized ZnFe₂O₄/ZnIn₂S₄ nanosheet stereoscopic films for exceptional visible light photocatalytic H₂ evolution performance, *Nanoscale* 9 (2017) 5912–5921.
- [19] Q.Y. Tian, W. Wu, J. Liu, Z.H. Wu, W.J. Yao, J. Ding, C.Z. Jiang, Dimensional heterostructures of 1D CdS/2D ZnIn₂S₄ composites with 2D graphene: designed synthesis and superior photocatalytic performance, *Dalton Trans.* 46 (2017) 2770–2777.
- [20] X. Chen, L. Li, W.Z. Zhang, Y.X. Li, Q. Song, L. Dong, Fabricate globular flower-like CuS/CdIn₂S₄/ZnIn₂S₄ with high visible light response via microwave-assisted one-step method and its multipathway photoelectron migration properties for hydrogen evolution and pollutant degradation, *ACS Sustain. Chem. Eng.* 4 (2016) 6680–6688.

- [22] L. Ye, Z.H. Li, Rapid microwave-assisted syntheses of reduced graphene oxide (RGO)/ZnIn₂S₄ microspheres as superior noble-metal-free photocatalyst for hydrogen evolutions under visible light, *Appl. Catal. B: Environ.* 160 (2014) 552–557.
- [23] Y. Su, Z. Zhang, H. Liu, Y. Wang, Cd_{0.2}Zn_{0.8}S@UiO-66-NH₂ nanocomposites as efficient and stable visible-light-driven photocatalyst for H₂ evolution and CO₂ reduction, *Appl. Catal. B: Environ.* 200 (2017) 448–457.
- [24] Q. Li, C. Cui, H. Meng, J.G. Yu, Visible-light photocatalytic hydrogen production activity of ZnIn₂S₄ microspheres using carbon quantum dots and platinum as dual Co-catalysts, *Chem. Asian J.* 9 (2014) 1766–1770.
- [25] S. Castarlenas, C. Téllez, J. Coronas, Gas separation with mixed matrix membranes obtained from MOF UiO-66-graphite oxide hybrids, *J. Membr. Sci.* 526 (2017) 205–211.
- [26] L. Wei, Y.J. Chen, Y.P. Lin, H.S. Wu, R.S. Yuan, Z.H. Li, MoS₂ as non-noble-metal co-catalyst for photocatalytic hydrogen evolution over hexagonal ZnIn₂S₄ under visible light irradiations, *Appl. Catal. B: Environ.* 144 (2014) 521–527.
- [27] L. Shi, P.Q. Yin, Y.M. Dai, Synthesis and photocatalytic performance of ZnIn₂S₄ nanotubes and nanowires, *Langmuir* 29 (2013) 12818–12822.
- [28] N.S. Chaudhari, S.S. Warule, B.B. Kale, Architecture of rose and hollow marigold-like ZnIn₂S₄ flowers: structural, optical and photocatalytic study, *RSC Adv.* 4 (2014) 12182–12187.
- [29] N.S. Chaudhari, A.P. Bhirud, R.S. Sonawane, L.K. Nikam, S.S. Warule, V.H. Rane, B.B. Kale, Ecofriendly hydrogen production from abundant hydrogen sulfide using solar light-driven hierarchical nanostructured ZnIn₂S₄ photocatalyst, *Green Chem.* 13 (2011) 2500–2506.
- [30] B. Gao, L.F. Liu, J.D. Liu, F.L. Yang, Photocatalytic degradation of 2,4,6-tribromophenol over Fe-doped ZnIn₂S₄: Stable activity and enhanced debromination, *Appl. Catal. B: Environ.* 129 (2013) 89–97.
- [31] J. Ding, Z.Q. Yang, C. He, X.W. Tong, Y. Li, X.J. Niu, H.G. Zhang, UiO-66(Zr) coupled with Bi₂MoO₆ as photocatalyst for visible-light promoted dye degradation, *J. Colloid Interface Sci.* 497 (2017) 126–133.
- [32] J. Cao, Q.Y. Liu, D.L. Han, S. Yang, J.H. Yang, T.T. Wang, H.F. Niu, Highly enhanced photocatalytic properties of ZnS nanowires-graphene nanocomposites, *RSC Adv.* 4 (2014) 30798–30806.
- [33] W. Chen, T.Y. Liu, T. Huang, X.H. Liu, J.W. Zhu, G.R. Duan, X.J. Yang, One-pot hydrothermal route to synthesize the ZnIn₂S₄/g-C₃N₄ composites with enhanced photocatalytic activity, *J. Mater. Sci.* 50 (2015) 8142–8152.
- [34] S. Ham, Y. Kim, M.J. Park, B.H. Hong, D.J. Jang, Graphene quantum dots-decorated ZnS nanobelts with highly efficient photocatalytic performances, *RSC Adv.* 6 (2016) 24115–24120.
- [35] C. Mondal, M. Ganguly, J. Pal, A. Roy, J. Jana, T. Pal, Morphology controlled synthesis of SnS₂ nanomaterial for promoting photocatalytic reduction of aqueous Cr(VI) under visible light, *Langmuir* 30 (2014) 4157–4164.
- [36] R.W. Liang, F.F. Jing, L.J. Shen, N. Qin, L. Wu, MIL-53(Fe) as a highly efficient bifunctional photocatalyst for the simultaneous reduction of Cr(VI) and oxidation of dyes, *J. Hazard. Mater.* 287 (2015) 364–372.
- [37] L. Shi, T. Wang, H.B. Zhang, K. Chang, X.G. Meng, H.M. Liu, J.H. Ye, An amine-functionalized iron (III) metal-organic framework as efficient visible-light photocatalyst for Cr(VI) reduction, *Adv. Sci.* 2 (2015) 1500006.
- [38] Z.H. Ai, Y. Cheng, L.Z. Zhang, J.R. Qiu, Efficient removal of Cr(VI) from aqueous solution with Fe@Fe₂O₃ core-shell nanowires, *Environ. Sci. Technol.* 42 (2008) 6955–6960.
- [39] Y.C. Zhang, J. Li, M. Zhang, D.D. Dionysiou, Size-tunable hydrothermal synthesis of SnS₂ nanocrystals with high performance in visible light-driven photocatalytic reduction of aqueous Cr(VI), *Environ. Sci. Technol.* 45 (2011) 9324–9331.
- [40] X.L. Wang, S.O. Pehkonen, A.K. Ray, Removal of aqueous Cr(VI) by a combination of photocatalytic reduction and coprecipitation, *Ind. Eng. Chem. Res.* 43 (2004) 1665–1672.
- [41] H.P. Chu, X.J. Liu, B.B. Liu, G. Zhu, W.Y. Lei, H.G. Du, J.Y. Liu, J.W. Li, C. Li, C.Q. Sun, Hexagonal 2H-MoSe₂ broad spectrum active photocatalyst for Cr(VI) reduction, *Sci. Rep.* 6 (2016) 35304.
- [42] D.F. Xu, B. Cheng, S.W. Cao, J.G. Yu, Enhanced photocatalytic activity and stability of Z-scheme Ag₂CrO₄-GO composite photocatalysts for organic pollutant degradation, *Appl. Catal. B: Environ.* 164 (2015) 380–388.
- [43] L. Gomathi Devi, S. Girish Kumar, K. Mohan Reddy, C. Munikrishnappa, Photo degradation of Methyl Orange an azo dye by Advanced Fenton Process using zero valent metallic iron: influence of various reaction parameters and its degradation mechanism, *J. Hazard. Mater.* 164 (2009) 459–467.
- [44] T.W. Chen, Y.H. Zheng, J.M. Lin, G.N. Chen, Study on the photocatalytic degradation of methyl orange in water using Ag/ZnO as catalyst by liquid chromatography electrospray ionization ion-trap mass spectrometry, *J. Am. Soc. Mass Spectr.* 19 (2008) 997–1003.
- [45] C. Baiocchi, M.C. Brusino, E. Pramauro, A.B. Prevot, L. Palmisano, G. ; Marci, Characterization of methyl orange and its photocatalytic degradation products by HPLC/UV-VIS diode array and atmospheric pressure ionization quadrupole ion trap mass spectrometry, *Int. J. Mass Spectrom.* 214 (2002) 247–256.
- [46] W. Qin, T.Q. Chen, T. Lu, D.H.C. Chua, L.K. Pan, Layered nickel sulfide-reduced graphene oxide composites synthesized via microwave-assisted method as high performance anode materials of sodium-ion batteries, *J. Power Sources* 302 (2016) 202–209.
- [47] S.H. Park, H.K. Kim, S.B. Yoon, C.W. Lee, D. Ahn, S.I. Lee, K.C. Roh, K.B. Kim, Spray-assisted deep-frying process for the in situ spherical assembly of graphene for energy-storage devices, *Chem. Mater.* 27 (2015) 457–465.
- [48] S. Bashkova, T.J. Bandosz, Insight into the role of the oxidized graphite precursor on the properties of copper-based MOF/graphite oxide composites, *Microporous Mesoporous Mater.* 179 (2013) 205–211.
- [49] H. Zhou, X.Q. Liu, J. Zhang, X.F. Yan, Y.J. Liu, A.H. Yuan, Enhanced room-temperature hydrogen storage capacity in Pt-loaded graphene oxide/HKUST-1 composites, *Int. J. Hydrogen Energy* 39 (2014) 2160–2167.
- [50] M. Wickenheisser, A. Herbst, R. Tannert, B. Milow, C. Janiak, Hierarchical MOF-xerogel monolith composites from embedding MIL-100(Fe,Cr) and MIL-101(Cr) in resorcinol-formaldehyde xerogels for water adsorption applications, *Microporous Mesoporous Mater.* 215 (2015) 143–153.